Combustion Science and Technology

INTERACTION BETWEEN COUNTERFLOW FLAMES OVER BINARY TSUJI BURNERS ARRANGED IN SIDE-BY-SIDE

DA-DA CHEN [a] , SHIN-SHEN TSA [a] & CHIUN-HSUN CHEN [a]

[a] Department of Mechanical Engineering , National Chiao Tung University , HsinChu, Taiwan
Published online: 25 Jan 2007.

PLEASE SCROLL DOWN FOR ARTICLE

and other liabilities whatsoever or howsoever caused arising directly or indirectly in connection with, in relation to or arising out of the use of the Content.

This article may be used for research, teaching, and private study purposes. Any substantial or systematic reproduction, redistribution, reselling, loan, sub-licensing, systematic supply, or distribution in any form to anyone is expressly forbidden. Terms & Conditions of access and use can be found at http://www.tandfonline.com/page/terms-and-conditions

Taylor & Francis
Taylor & Francis Group

INTERACTION BETWEEN COUNTERFLOW FLAMES OVER BINARY TSUJI BURNERS ARRANGED IN SIDE-BY-SIDE

DA-DA CHEN
SHIN-SHEN TSA
CHIUN-HSUN CHEN[*]

Department of Mechanical Engineering, National
Chiao Tung University, HsinChu, Taiwan

This numerical study modifies Tsa and Chen's preliminary combustion model (2003) by using a multi-block grid to investigate further the interaction of flames over binary Tsuji burners. The effects of inter-cylinder spacing (L) and inflow velocity (U_{in}) are investigated. A wider inter-cylinder spacing generally corresponds to lower flame transition velocity, associated with the transformation of the envelope flame into the wake flame. However, the combustion efficiency increases with L. The twin envelope diffusion flames merge into a larger envelope diffusion flame completely when L is equal to or less than 1.5D. Only one vortex is present behind each burner when L = 1.5D or 2D. However, no vortex is present when L = 1.2D. When L is equal to or greater than 3.5D, no interference occurs between the two flames. The mechanism of control of the interaction between twin counterflow diffusion flames involves oxygen deficiency between the dual flames. In the case of varying U_{in} at fixed L = 3D, the dual envelope diffusion flames transform into dual wake flames as U_{in} increases to 0.79 m/sec. The dual wake flames

[*]Address correspondence to chchen@mail.nctu.edu.tw

are extinguished as U_{in} increases further to 1.96 m/sec. Increasing the inflow velocity can enhance the interaction between dual envelope flames. A larger inflow velocity yields a lower flame temperature due to the flame stretch effect. Three vortices are present behind each cylinder when the flames are at the near-extinction velocity. For a fixed inter-cylinder spacing, the dual flames tend to attract each other normally. However, the dual flames repel each other as the inflow velocity increases to the near-extinction limit.

Keywords: dual envelope diffusion flame, dual wake flame, flame stretch, multi-block grid

INTRODUCTION

This study numerically investigates the interaction between the flames over two porous cylindrical burners, as functions of the distance between them and the inflow velocity. This is an extension of Tsa and Chen's study (2003), which numerically investigates flame lift-off phenomena over a single Tsuji burner, and a corresponding experiment for investigating the interference phenomena associated with twin flames over two Tsuji burners arranged side-by-side (Chen, 2003). Therefore, this work seeks to solve the corresponding flame interaction numerically. However, the flow field is much more complicated than that in Tsa and Chen's study (2003) since one more burner is added in the test section. Therefore, a new grid generation technique is developed to solve the double-burner problem.

Flame interaction phenomena over binary Tsuji burners were not identified until 1995. Xu (1995) and Wang (1998) used side-by-side and staggered arrangements to determine experimentally flame transition velocity and flame extinction velocity. The parameters varied were the inter-cylinder spacing and the angle of inclination between the inflow velocity and the cylinder plane. However, their experiments did not measure the temperature, concentration of the species, and the flow field.

Toong (1961) utilized two cylindrical fuel plates to simulate the interactive combustion between dual droplets in a forced convective environment. He found that the rate of evaporation or sublimation at the fuel surface increases as the space between the plates declines, while the rate of combustion at the flame front decreases. When the distance between the droplets is relatively large, the two flames that surround the droplets remain separated, although their shapes are distorted by an increase in the stream velocity. When the droplets are closer, the two flames merge and then they burn like a single large droplet at a lower rate.

Umemura (1994) comprehensively reviewed the interactive droplet vaporization and combustion phenomena. He concluded that the useful concepts in the generalized asymptotic theory are the influence distance of a test droplet, the dimension index of the droplet ensembles and the local group combustion number. They are all related to the inter-droplet spacing through the ordering factor γ, which characterizes the order of magnitude of the rate of vaporization of the test droplet as a function of the gas-to-liquid density ratio. In the burning problem with two identical droplets, the rate of vaporization of each droplet is suppressed by interaction, and the total vaporization rate of the two droplets exceeds that of a single droplet with the same total volume.

Dong et al. (2003) experimentally investigated the heat transfer characteristics of a row of three premixed, laminar, butane/air flame jets, impinging on a water-cooled flat plate. They found that the area-averaged heat flux can be reduced at small inter-jet spacing. The heat transfer is highest when the inter-jet spacing is at a moderate value of 5D, at which both the local and maximum heat fluxes reach their maximum values. The lowest area-averaged heat flux is obtained as the interjet spacing is 2.6D.

Abdalla et al. (1999) presented an extensive set of results and a corresponding discussion on flame length in relation to experimental work on two-jet acetylene flame systems. The systems included parallel, divergent and convergent jet configurations. As the separation between the jets decreases, the availability of the air to the two streams of fuel gas declines and flame length increases for a given Reynolds number in the parallel jet configuration.

Annamalai et al. (1994) comprehensively reviewed the subject on the combustion of interacting coal particles. They showed that the group combustion number must be derived in terms of a ratio of sphere diameter to inter-particle spacing. Consequently, a correlation between these parameters is obtained that is suitable for relating group combustion theory to particle array studies.

Kharbat (1992) experimentally studied the effect of inter-candle spacing on the candle mass burning rate. The minimum time required to burn 40% of the mass of a candle is determined by the competing effects of free convection and oxygen deficiency.

Mohr et al. (1996) clarified the previously unknown interaction between two Radial Jet Reattachment Combustion (RJRC) flames in a pseudo-array configuration. The flow structure of the two RJRC flames depends closely on the inter-nozzle spacing. In the region of interaction

between each pair of nozzles, the local heat flux was a strong function of nozzle spacing. The maximum heat flux and the impingement surface temperatures were measured at an inter-nozzle spacing of $S/R_0 = 8.0$, while the corresponding minimum values were measured at $S/R_0 = 5.0$. The optimal spacing between the two nozzles was observed in the region of moderate interaction ($6.0 < S/R_0 < 9.0$). Very high values of local heat flux were obtained with the RJRC nozzle pair, and the area of high heat flux became wider as the inter-nozzle spacing increased.

From the previous literature review, it can be found that the interaction between the flames strongly depends on the distance between them. Therefore, this study extends Tsa and Chen's single burner combustion model (2003) to dual ones, and focuses on the relationship between the flame interaction and inter-cylinder spacing of two porous cylinders, arranged as illustrated in Figure 1. The arrangement is similar to the experimental setup of Chen (2003), in which two cylindrical burners are mounted side-by-side in a wind tunnel. This combustion model is further improved by incorporating a multi-block grid system into the original combustion model. However, the chemical kinetics mechanism used is one-step rather than four-step as in Tsa and Chen (2003) due
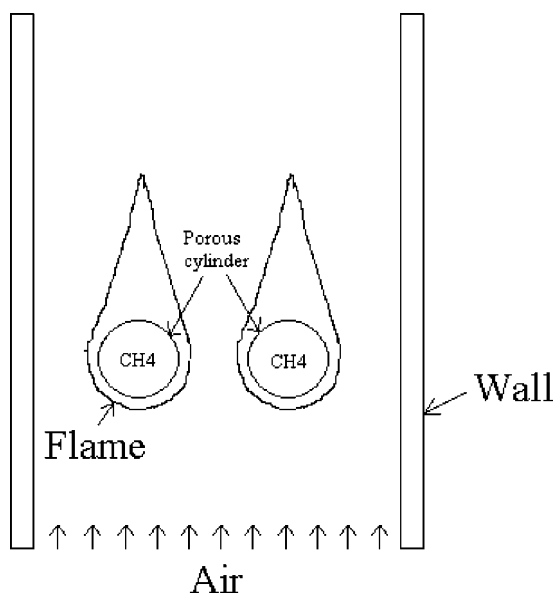

**Figure 1.** Schematic configuration of the physical problem.

to uncontrollable required computational memory capacity. The varied parameters are the inter-cylinder spacing (L) and the inflow velocity (U_{in}). The main purpose of this work is to investigate under what conditions the two flames can exist separately without interaction, and subsequently analyzes the characteristics of the dual flames as they are merged. Also, each possible flame configuration during the flame transition process can be identified: the dual envelope flames are transformed into a single larger flame or dual wake flames over the porous cylinders.

MATHEMATICAL MODEL

Several assumptions are made to increase the tractability of the problem.

1. The flow is steady, two-dimensional, and laminar, according to Stokes' hypothesis.
2. Radiant heat transfer is neglected.
3. The viscous dissipation and compression work are neglected owing to the low speed of the combustion problem.
4. The ideal gas law can be applied to the gas mixture with constant and equal specific heats, equal diffusion coefficients, and constant Prandtl and Lewis numbers.
5. The average molecular weight is constant.
6. The temperature on the surface of the cylinder is constant.
7. The symmetry condition is assumed at the mid-plane between two cylinders. This assumption may not be appropriate because it is known that the unsteady alternating vortices will commence to appear as Re > 40, destroying the symmetrical assumption since then. However, this study retains this assumption for simplicity.
8. The gas phase chemistry is described by a one-step overall chemical reaction, rather than the four-step chemical kinetics adopted by Tsa and Chen (2003). It is because this study has much more complicated flow configuration due to the arrangement of dual burners and the use of multiple-step chemical reactions will lead to an uncontrollable computational memory requirement.

   The one-step overall chemical reaction is that gaseous fuel reacts with an oxidizer to form products and release heat:

$$1 \text{ Kg[Methane]} + f \text{ Kg[Oxidizer]} \rightarrow (1+f) \text{ Kg[Product]} + Q \text{ KJ[Heat]} \tag{1}$$
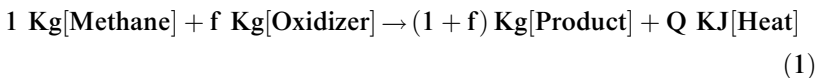
where f and Q represent the stoichiometric oxidizer/fuel mass ratio and the heat of combustion per unit mass of fuel, respectively. Therefore, the relationship between mass and energy source terms is,

$$\overline{\omega}_F = \overline{\omega}_o/f = -\dot{\overline{Q}}/Q \tag{2}$$

The rate equation is assumed to depend on concentration and temperature, which they are expressed by the second-order Arrhenius' law. The rate equation for fuel is

$$\overline{\omega}_f = -\overline{B}\overline{\rho}^2 Y_f Y_o \exp(-\overline{E}/R^0\overline{T}) \tag{3}$$

where $\overline{B}$ and $\overline{E}$ are the frequency factor and the activation energy, respectively.

Since the combustion model is solved non-dimensionally, a normalization procedure is implemented in advance. The non-dimensional variables are defined as,

$$x = \frac{\overline{x}}{R}, \; y = \frac{\overline{y}}{R}, \; u = \frac{\overline{u}}{U_{in}}, \; v = \frac{\overline{v}}{U_{in}}, \; \rho = \frac{\rho}{\rho^*}, \; p = \frac{\overline{P} - \overline{P}_{rc}}{\rho^* U_{in}^2}, \; \mu = \frac{\overline{\mu}}{\mu^*},$$

$$Re = \frac{\rho^* U_{in} R}{\mu^*}, \; Pr = \frac{\overline{\mu} C_p}{\overline{k}}, \; Le = \frac{\overline{k}}{\overline{\rho} C_p \overline{D}}, \; T = \frac{\overline{T}}{T^*}, \; Q = \frac{\overline{Q}}{C_p T^*}, \; E = \frac{\overline{E}}{R^0 T^*},$$

$$Da = \frac{R/U_{in}}{1/(\rho^* \overline{B} \exp(-\overline{E}/R^0 T^*))}, \; \dot{m} = \frac{\overline{\dot{m}}}{\rho^* U_{in}}, \; -f_w = \left(\frac{v_w}{U_{in}}\right)\left(\frac{Re}{2}\right)^{0.5} \tag{4}$$

where U_{in} is the inflow velocity, R the cylinder radius, and T^* the reference temperature, the arithmetic average of ambient and adiabatic flame temperatures.

Based on the non-dimensional variables and parameters just defined, the resultant dimensionless governing equations and boundary conditions are as follows.

Non-dimensional Governing Equations

Continuity equation:

$$\frac{\partial(\rho u)}{\partial x} + \frac{\partial(\rho v)}{\partial y} = 0 \tag{5}$$

X-momentum equation:

$$\rho u \frac{\partial u}{\partial x} + \rho v \frac{\partial u}{\partial y} = -\frac{\partial p}{\partial x} + \frac{\partial}{\partial x} \left\{ \frac{\mu}{Re} \left[2\frac{\partial u}{\partial x} - \frac{2}{3} \left(\frac{\partial u}{\partial x} + \frac{\partial v}{\partial y} \right) \right] \right\}$$
$$+ \frac{\partial}{\partial y} \left[\frac{\mu}{Re} \left(\frac{\partial u}{\partial y} + \frac{\partial v}{\partial x} \right) \right] \tag{6}$$

Y-momentum equation:

$$\rho u \frac{\partial v}{\partial x} + \rho v \frac{\partial v}{\partial y} = -\frac{\partial p}{\partial y} + \frac{\partial}{\partial y} \left\{ \frac{\mu}{Re} \left[2\frac{\partial v}{\partial x} - \frac{2}{3} \left(\frac{\partial u}{\partial x} + \frac{\partial v}{\partial y} \right) \right] \right\}$$
$$+ \frac{\partial}{\partial x} \left[\frac{\mu}{Re} \left(\frac{\partial v}{\partial x} + \frac{\partial u}{\partial y} \right) \right] \tag{7}$$

Energy equation:

$$\rho u \frac{\partial T}{\partial x} + \rho v \frac{\partial T}{\partial y} = \frac{1}{Re\,Pr} \left[\frac{\partial}{\partial x} \left(\mu \frac{\partial T}{\partial x} \right) + \frac{\partial}{\partial y} \left(\mu \frac{\partial T}{\partial y} \right) \right] - Q\dot{\omega}_f \tag{8}$$

Fuel species equation:

$$\rho u \frac{\partial Y_f}{\partial x} + \rho v \frac{\partial Y_f}{\partial y} = \frac{1}{Re\,Pr\,Le} \left[\frac{\partial}{\partial x} \left(\mu \frac{\partial Y_f}{\partial x} \right) + \frac{\partial}{\partial y} \left(\mu \frac{\partial Y_f}{\partial y} \right) \right] + \dot{\omega}_f \tag{9}$$

Oxidizer species equation:

$$\rho u \frac{\partial Y_o}{\partial x} + \rho v \frac{\partial Y_o}{\partial y} = \frac{1}{Re\,Pr\,Le} \left[\frac{\partial}{\partial x} \left(\mu \frac{\partial Y_o}{\partial x} \right) + \frac{\partial}{\partial y} \left(\mu \frac{\partial Y_o}{\partial y} \right) \right] + f\dot{\omega}_f \tag{10}$$

where

$$\dot{\omega}_f = -Da\rho^2 Y_f Y_o \exp(E - E/T) \tag{11}$$

is the non-dimensional fuel reaction rate.

The equation of state is,

$$\rho = 1/T \tag{12}$$

and the viscosity variation with temperature is taken as

$$\mu = T^{0.75} \tag{13}$$

The parameters appearing in the preceding equations can be found in nomenclature for their mathematical definitions.

Non-dimensional Boundary Conditions

In Figure 2, the non-dimensional boundary conditions are
At $x = x_{in}$:

$$u = 1, \, v = 0, \, T = 0.24, \, Y_f = 0, Y_o = 0.233 \tag{14}$$

At $x = x_{out}$:

$$\frac{\partial u}{\partial x} = 0, \, v = 0, \, \frac{\partial T}{\partial x} = \frac{\partial Y_f}{\partial x} = \frac{\partial Y_o}{\partial x} = 0 \tag{15}$$

At $y = y_{wall}$:

$$u = v = 0, \, \frac{\partial T}{\partial y} = \frac{\partial Y_f}{\partial y} = \frac{\partial Y_o}{\partial y} = 0 \tag{16}$$
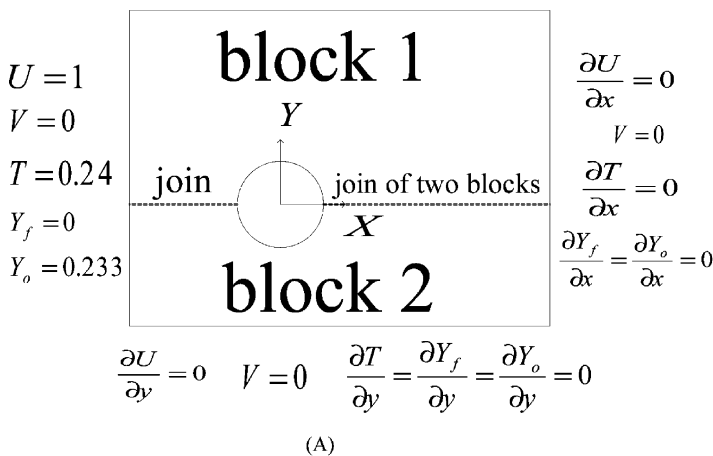
(A)

(B)

Figure 2. (A) The boundary conditions of the physical domain and of the multi-block grid. (B) The grid distributions ($218 \times 115 \times 2$).
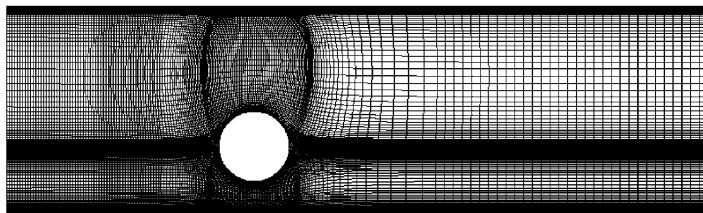
At $y = -\dfrac{L}{2R}$ (symmetric line):

$$\frac{\partial \mathbf{u}}{\partial \mathbf{y}} = 0, \ \mathbf{v} = 0, \ \frac{\partial T}{\partial y} = \frac{\partial Y_f}{\partial y} = \frac{\partial Y_o}{\partial y} = 0 \tag{17}$$

At $-1 < \mathbf{x} \le 1$, $\sqrt{\mathbf{x}^2 + \mathbf{y}^2} = 1$:

$$\mathbf{v}_t = 0, \ \mathbf{v}_n = -f_w (2/\text{Re})^{0.5}, \ T_w = 0.32, \ \dot{m}_w = v_n \rho_w$$

$$\dot{m}_w Y_{fw} = \dot{m}_w + \frac{1}{\text{Re Pr Le}} \mu \frac{\partial Y_f}{\partial n}|_w \tag{18}$$

$$\dot{m}_w Y_{ow} = \frac{1}{\text{Re Pr Le}} \mu \frac{\partial Y_o}{\partial n}|_w$$

Note that the non-dimensional velocity of ejection of the fuel, $-f_w$, from the cylinder is adopted from the experimental data of Tsuji and Yamaoka (1967).

Numerical Algorithm and Solution Procedure

The configuration of the flow field, as depicted in Figure 1, is irregular. Therefore, a body-fitted coordinate system, generated by a grid generation approach (Thomas and Middecoff, 1980), is applied. The equations of grid generation are the same as those in Chen and Weng (1990), but the concept of the multi-block grid is introduced in the computation performed here. Using such a concept, the physical domain is transformed into a computational domain, consisting of equally spaced, square grids.

Figure 2 depicts the physical domain, which is a multiply connected region with obstacle(s) in the interior of the field, i.e., the region has interior boundaries. This configuration differs from the simply connected region in Chen and Weng (1990), thus, a new type of grid must be selected. In general, four types of grid can be used for a multiply connected region: they are O-type, C-type, H-type, and multi-block grids. The O-type and C-type grids are not suited to the physical domain of interest here because of the inherent sparseness of the grid cells near the outer boundary or the wall. The velocity gradient near the tunnel wall is very large because of the no-slip condition, so the grid near the tunnel wall must be fine. Two singular points are present in the H-type grid for the physical domain used here. Therefore, a multi-block grid is selected herein.

Two straight branch cuts parallel to the tunnel wall are introduced to separate the physical domain into two parts (Figure 2). The two branch cuts are separately perpendicular to the inlet and outlet boundaries, and

pass through the origin. They are specified by y = 0. Two simply connec-
ted regions, each with a semi circular hollow, are thus obtained, and the
two blocks are connected to each other to form the physical domain.
Accordingly, the grid generation method above can be applied to form
two grid systems with different lengths at the inlet and the outlet. The
lower grid system is in the negative y half-plane, and the upper one is
in the positive y half-plane. Finally, Figure 2 depicts the complete two-
block grid with its origin at the center of a cylinder. The details, such
as the branch cuts, point- and derivatives-correspondence, can be
referred to Tsa et al. (2003).

The upstream and downstream positions are determined by perform-
ing many numerical experiments to meet the requirement that the apply-
ing boundary conditions at these positions should not impact flame
structures. Besides, from the observation in corresponding experiment
(Chen, 2003), it is found that distance between the wall and porous cylin-
der not to influence the results is greater than 2D. The numerical results
show the same conclusion as well. As for the upstream and downstream
boundaries, the previous numerical study by Chen and Weng (1990) has
ensured that $x_{in} = -7$, $x_{out} = 13$ for the computational domain is large
enough not to influence the flame around the burners. A set of numerical
tests is performed to further ensure that the resultant solutions are inde-
pendent of the grid. Table 1 presents test results. The cases shown in the
first column are the same as those in Figure 8, which will be discussed
later. If the number of cells exceeds $218 \times 115 \times 2$, then the variation in
the resultant peak temperature, the variable most sensitive to the size of
the grid, over the entire computational domain becomes insignificant.
Therefore, this study chooses $218 \times 115 \times 2$ grid cells.

Table 1. Grid test results

	$62 \times 27 \times 2$	$164 \times 85 \times 2$	$218 \times 115 \times 2$	$402 \times 221 \times 2$	$864 \times 501 \times 2$
Case A1	2297	2195	2181	2182	2183
Case A2	2286	2161	2174	2172	2174
Case A3	2266	2156	2154	2151	2149
Case A4	2250	2108	2130	2126	2131
Case A5	2226	2148	2116	2120	2120
Case A6	2205	2132	2105	2105	2104
Case A7	2196	2066	2101	2102	2096

The peak temperature in the whole computational domain (unit: K).

The configuration of the multi-block structure, as shown in Figure 2, is divided into two blocks. The computation in the dual cylinder case begins by making a hot profile around the burner. Then, block 1 (the upper block) is solved in odd iterations and block 2 (the lower block) in even iterations. In odd iterations, only U, V, T, Y_f, and Y_o are calculated. P′ (ΔP), pressure, and velocity corrections are not calculated in odd iterations, but they are done in even iterations. Thus only the velocity, temperature, and species concentrations of block 1 are calculated in odd iterations, while the velocity, temperature, and species concentrations of block 2 are calculated in even iterations. Corrected pressure, the pressure correction, and the velocity correction for both blocks are computed only in even iterations.

The branch cuts connect blocks 1 and 2, so two layers of grid points are always present at such cuts. One layer belongs to block 1, and the other belongsto block 2. At branch cuts, two grid points are present at a single location, and belong to blocks 1 and 2. Accordingly, the physical propertiesshould be the same at both grid points, and the discrepancies between the binal points significantly affect the solution's precision. Therefore, the criteria for identifying the convergence of the computations is that the maximum temperature difference between each binal point at the branch cuts is less than 10 K and the maximum x-direction velocity difference between each binal point at the branch cuts is below $0.005 \, U_{in}$ and the maximum y-direction velocity difference between each binal point at the branch cuts is under $0.002 \, U_{in}$. Besides, when the maximum residual of temperatures, x-direction velocities, and y-direction velocities in blocks 1 and 2 are simultaneously less than 0.001, the iteration procedure is terminated and the results are printed. Restated, when $\left| R_{u,block1} \right|_{max}$, $\left| R_{v,block1} \right|_{max}$, $\left| R_{T,block1} \right|_{max}$, $\left| R_{u,block2} \right|_{max}$, $\left| R_{v,block2} \right|_{max}$, and $\left| R_{T,block2} \right|_{max}$ are all less than 0.001, $\left| \Delta T_{branch\_cut} \right|_{max}$ is less than 10 K, $\left| \Delta U_{branch\_cut} \right|_{max}$ is less than $0.005 \, U_{in}$, and $\left| \Delta V_{branch\_cut} \right|_{max}$ is less than $0.002 \, U_{in}$, the final converged solutions are obtained. Figure 3 presents the complete flow chart of the computational process, which took approximately 10 hours to yield a converged solution in the twin burner case.

RESULTS AND DISCUSSION

The gaseous fuel used was methane (CH_4) and the ambient oxidizer was air. The thermodynamics, transport, and chemical kinetic data for the

```
┌─────────────────────────────────────────────┐
│        Make a hot profile around the burner   │
└─────────────────────────────────────────────┘
                        │
                        ▼
┌─────────────────────────────────────────────┐
│   Solve_U,V,T,Yf, and_Yo _at_block_1          │
└─────────────────────────────────────────────┘
                        │
                        ▼
┌─────────────────────────────────────────────┐
│  Deliver the boundary values to block 2 at    │
│                branch cuts                     │
└─────────────────────────────────────────────┘
                        │
                        ▼
┌─────────────────────────────────────────────┐
│   Solve U, V, T, Yf, and Yo at block 2 and     │
│   calculate P`, pressure correction, and       │
│       velocity correction at both blocks        │
└─────────────────────────────────────────────┘
                        │
                        ▼
┌─────────────────────────────────────────────┐
│  Deliver the boundary values to block 1 at    │
│                branch cuts                     │
└─────────────────────────────────────────────┘
                        │
                        ▼
┌─────────────────────────────────────────────┐
│                   Check if                     │
└─────────────────────────────────────────────┘
```

Check if

$$|R_{u,block1}|_{max}, |R_{v,block1}|_{max}, |R_{T,block1}|_{max}, |R_{u,block2}|_{max}, |R_{v,block2}|_{max}, and\_|R_{T,block2}|_{max} \leq 0.001$$

$$and\_|\Delta U_{branch\_cut}|_{max} \leq 0.005 U_{in}, |\Delta V_{branch\_cut}|_{max} \leq 0.002 U_{in}, and\_|\Delta T_{branch\_cut}|_{max} \leq 10K$$
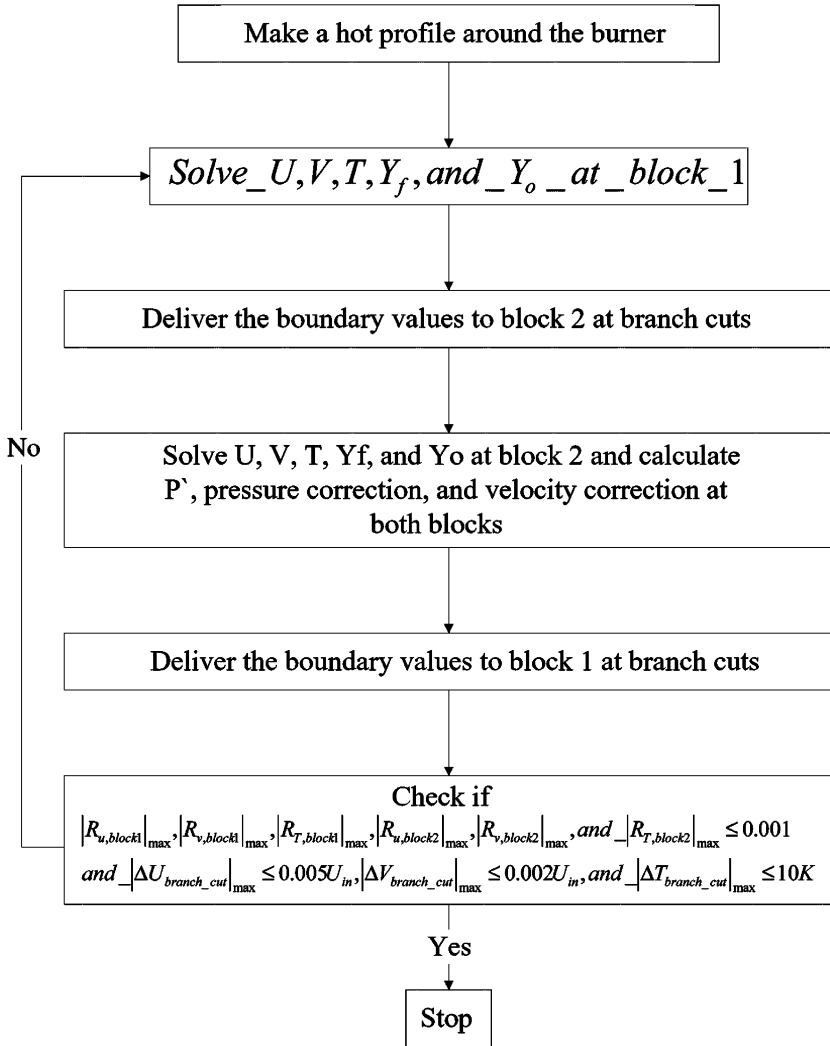
Yes

Stop

Figure 3. Flow chart for the multi-block computational scheme.

dual burner case were all taken from the work of Chen and Weng (1990), and are listed in Table 2.

Two parametric studies, based on separately varying the inter-cylinder spacing (L) and inflow velocity (U_{in}) at the fixed non-dimensional full cylinder surface fuel-ejection rate, $-f_w = 0.1$.

Table 2. Property values

Name	Symbol	Value	Unit
Ambient temperature	$\overline{T}_a$	300	K
Reference temperature	T^*	1250	K
Density (reference)	ρ^*	0.2835	Kg/m^3
Kinematic viscosity (reference)	U^*	1.69 E-4	m^2/sec
Thermal diffusivity (reference)	α^*	2.36 E-4	m^2/sec
Specific heat (reference)	C_p	1.351	$KJ/(Kg \times K)$
Cylinder surface temperature	$\overline{T}_w$	400	K
Oxidizer velocity	U_{in}	variable	m/sec
Fuel-ejection velocity	v_w	0.013	m/sec
Cylinder radius	R	0.015	m
Air molecular weight (reference)	M_{air}	28.97	Kg/Kmole
Atmospheric pressure at STP condition	$\overline{P}_{rc}$	101325	Pa

Note that this study fixes the distance between the burner and wall and changes the spacing between cylinders in the computational domain. From the experimental observations and numerical computations, it is found that distance between the wall and the porous cylinder should not influence the results when it is greater than 2 D, where D is burner diameter.

The fixed distance between the wall and the porous cylinder is 4D and the inter-cylinder spacing (L) is varied from 1.2D to 4D. From the literature review, the inter-cylinder spacing is expected to be the parameter that dominates the flame interaction/interference phenomena over dual Tsuji burners.

Increasing U_{in} augments the flame stretch rate, k_s, defined as $2U_{in}/R$. The inflow velocity varies from 0.2 m/sec to 1.955 m/sec. Comparisons are made with the experimental results of Wang (1998) and Chen (2003).

Comparisons with Related Experiments and Simulations

Comparison with Wang's Experimental Results (1998). Figure 4 shows the transition velocity, at which the envelope flame is transformed into a wake one, as a function of non-dimensional inter-cylinder spacing (L/D) in this simulation and Wang's experiments (1998). Notably, in Wang's set-up, the flames over the burners burn in the atmosphere, as two jets of N_2 are ejected from the two end sides of the burner, parallel
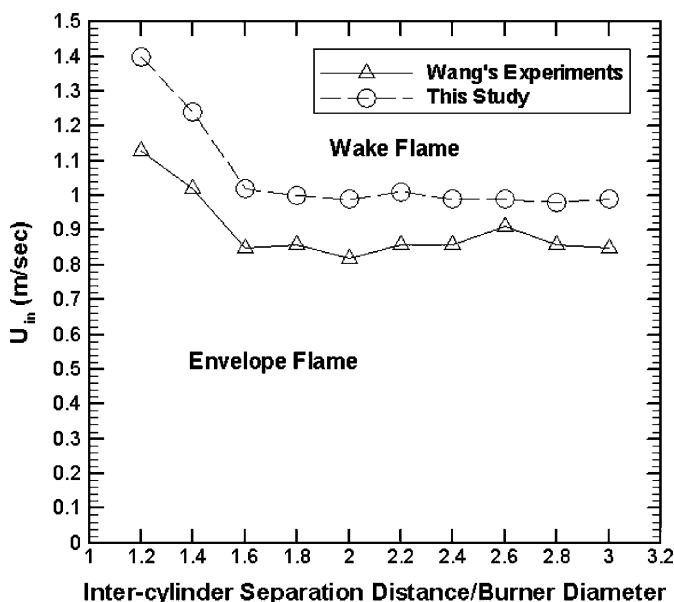
Figure 4. Flame transition curves from envelope flame to wake flame (Comparison with Wang's (1998) experimental measurements and $v_w = 0.46\,\text{cm/sec}$ and $D = 0.96\,\text{cm}$). (Using one-step LPG oxidation chemical kinetics model.)

to the main stream to prevent the induced air from affecting the process. The fuel used in this experiment was LPG (99%), where the corresponding chemical kinetics in this simulation are taken from Westbrook and Dryer (1981) and have the following form;

$$\omega_{C_3H_8} = 8.6 * 10^{11}\, T \exp\left(-\frac{30.0}{RT}\right) Y_{C_3H_8}^{0.1}\, Y_{O_2}^{1.65}$$

The diameter (D) of the burner is 0.96 cm and the blowing velocity along the burner surface is fixed at $v_w = 0.46\,\text{cm/s}$.

In general, a larger non-dimensional inter-cylinder spacing results in a lower transition velocity until a critical inter-cylinder separation distance, $L/D = 1.6$, is reached. When $L/D > 1.6$, the transition velocities are almost constant in both Wang's experiments (1998) and this work. Restated, the flame interaction/interference is not obvious when the inter-cylinder separation exceeds 1.6D. In the range $1.2D \le L \le 1.6D$, the transition velocity is approximately inversely proportional to the non-dimensional spacing. The qualitative trend in both studies is the same.

However, the maximum discrepancy between Wang's measurements (1998) and the predicted results is about 25%, mainly because Wang's burners (1998) were placed in open air and two N_2 gas jets were passing at the side ends of the burners, while the burners in this simulation were in a wind tunnel with solid walls. Also, this simulation is two dimensional, in other words, the flame over burner has no heat loss in the cylindrical axis direction. In Wang's experiment (1998), the burner length is finite and the boundaries of test section are nitrogen stream that it is inevitable to lose a great deal of heat to atmosphere. It can be termed as a three-dimensional effect, which contributes to the major discrepancy between predicted and measured results.

Comparison with Chen's Results (2003). Figure 5 compares the transition velocity in this present simulation with that obtained experimentally by the authors' colleague, Chen (2003). Figure 6 depicts Chen's experimental structure. Basically, the setup consists of a wind tunnel and a pair of porous sintered cylindrical burners. The wind tunnel is designed to provide a laminar, uniform oxidizer flow over the porous
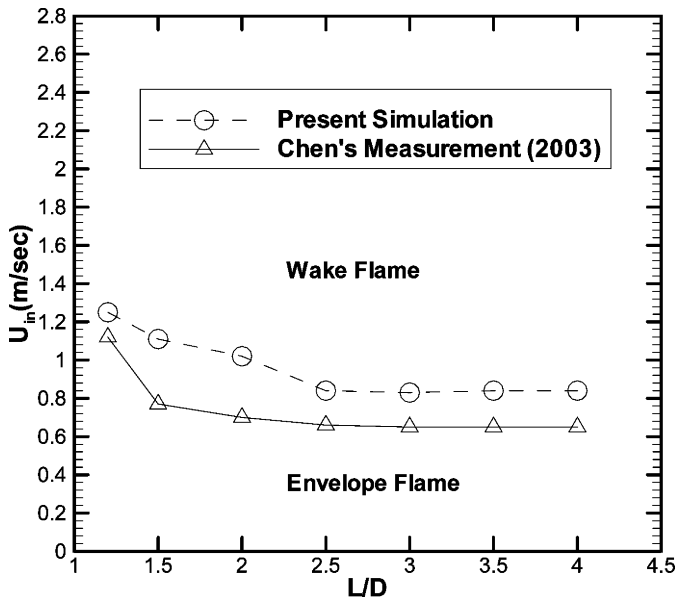
Figure 5. Comparison with Chen's corresponding flame transition curve (2003) for dual burners case (S = 360°).
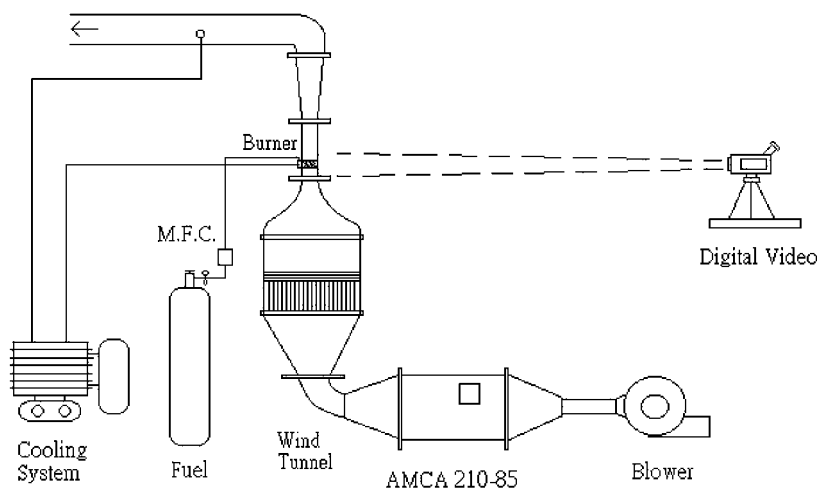
Figure 6. Schematic drawing of overall experimental system.

cylindrical burners, from which the gaseous fuels are ejected into the stream.

In Figure 5, the transition velocities are plotted against the non-dimensional spacing (L/D) at a fixed $-f_w = 0.25$ and a burner diameter (D) of 3 cm. This figure is similar to the preceding one (Figure 4), but the fuel used is methane and the burners are mounted in a closed test section instead of an open-air environment. In Chen's work (2003), the transition velocity drops rapidly as the inter-cylinder spacing increases from 1.2D to 1.5D. However, as the inter-cylinder spacing further increases, the flame transition velocity falls slowly until the spacing reaches 2.5D.

In this simulation, the transition velocity of the flame declines slowly as the inter-cylinder spacing increases from 1.2D to 2.5D. In this range, the discrepancy between the current predictions and Chen's measurements (2003) increases rapidly from a minimum to a maximum as the inter-cylinder spacing increases from 1.2D to 1.5D. Then, it declines slightly as the spacing further increases to 2D. As the inter-cylinder spacing increases from 2D to 2.5D, the difference becomes small. Furthermore, as the inter-cylinder spacing is increased beyond 2.5D, the flame transition velocity is nearly kept constant irrespective of this simulation or Chen's experiment (2003). Generally, the flame transition velocity declines as the inter-cylinder spacing increases. The trends in this present simulation are consistent with Chen's measurements (2003).

Figure 7 plots the temperature distributions along the symmetry line, $y = -L/2$. $X = 0$ is in the centers of the two cylinders and the positive x-axis represents the downstream axial direction. The temperature generally increases with X, especially in cases of intermediate inter-cylinder spacing. For both simulation and experiment, in the case of 1.2 D inter-cylinder spacing, the temperature initially declines monotonically as X increases until X reaches approximately 5 cm. Thereafter, the temperature increases slowly with X. The discrepancy between the simulation and experimental results is maximal at $X = 0$, and is about 300 K. The average difference is under 200 K.

When the inter-cylinder spacing increases to 2D, a sharp temperature rise begins at about $X = 2.3$ cm in the simulation. At $X \approx 11.3$ cm, the temperature reaches the maximum of about 2040 K, and then falls slightly downstream. This predicted temperature profile is quite different from that measured by Chen (2003), which increases gradually from 300 K at
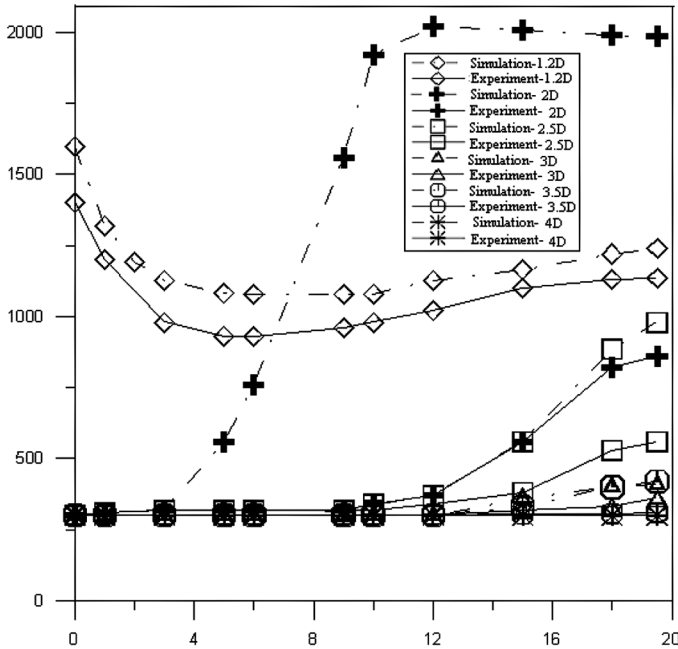

Figure 7. Temperature at the symmetric line versus axial distance for dual burners case (Comparison with Chen's corresponding experimental measurements (2003)). ($S = 360°$.)

X = 0 cm to 840 K at X = 20 cm. This extreme difference obtained with an inter-cylinder spacing of 2D results from the existence of the so-called biased bistable flow in the experiment (Zdravkovich, 1977). This phenomenon has not yet been satisfactorily explained. Based on assumptions of steady flow and symmetry (such that a half-plane computation was made), this simulation could not predict such a flow pattern.

As the inter-cylinder spacing increases to 2.5D, the temperature along the line of symmetry remains at the atmospheric temperature when X is less than eight, and the predicted profile is almost exactly the same as the measured one. Further downstream, the temperature increases with X, and the discrepancy between the simulation and measurements also increases. The maximum discrepancy is about 400 K at X = 19.5, and the mean discrepancy is less than 100 K. However, the simulation in the 2.5D case yields results that are very close to the measurements made in the 2D case of Chen's work (2003). Further increasing the inter-cylinder spacing to 3D greatly reduces the difference between the measurements and predictions, and the maximum discrepancy between them is then less than 60 K. The patterns of temperature rise versus X in the 2.5D and 3D inter-cylinder spacing cases are the same. However, the temperatures in the 3D inter-cylinder spacing case are much lower than those in the 2.5D case.

When the inter-cylinder spacing increases to 3.5D and 4D, the simulated and experimental temperature profiles are nearly the same. The temperatures along the X axis are almost the same, being atmospheric temperature, indicating that no flame interference occurs when the inter-cylinder spacing is equal to or larger than 3.5D.

In cases of an inter-cylinder spacing of over 1.2 D, the temperature along the line of symmetry increases downstream. The high-temperature zone far downstream is a thermal plume. In the case of 1.2 D inter-cylinder spacing, the temperature far upstream is very high – higher than the downstream temperature – because the two flame fronts merge. Except in the case without flame interaction, such as in the 3.5 D and 4 D cases, the simulated temperature always exceeds the temperature obtained experimentally by Chen (2003), perhaps because the chemical reaction simulated using one-step overall chemical kinetics is too fast, three dimensional effect pertains, and the thermocouple bead in the experiment has a quenching effect. However, the numerical error may cause the simulated temperature to be slightly lower than that measured at 3.5 D and 4 D inter-cylinder spacings. Finally, except in the 2 D

inter-cylinder spacing case, the discrepancies between the simulations and Chen's measurements (2003) are acceptable if the aforementioned reasons and the uncertainty caused by the thermocouple are considered.

Comparison with Previous Single Burner Simulations. The streamline and temperature profiles in Figure 8-A1 for the case of 4 D inter-cylinder separation distance are the same as those in Figure 8-A0, which is for a single burner. The reaction rate contours in this case (Figure 9-A1) are nearly the same as those in the single burner case (Figure 9-A0) as well. This similarity is also hold for the oxygen and fuel mass fraction contours; see Figures 10-A1 and 10-A0. Moreover, the streamline,
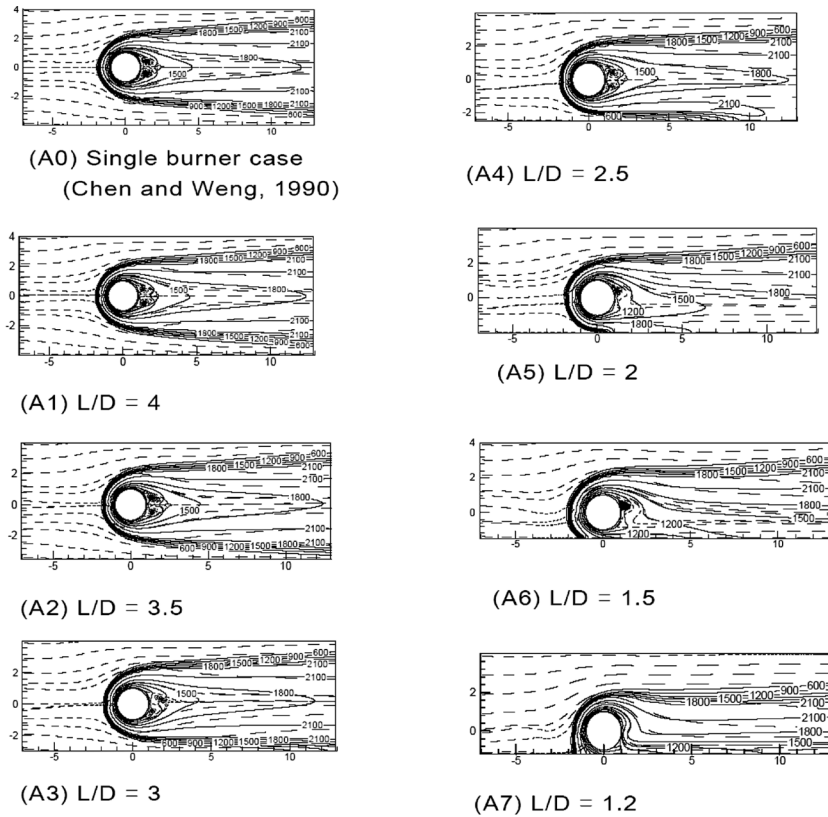

Figure 8. Series of streamline and temperature contour distributions in 0.2 m/sec inflow velocity condition (Re = 17.75 and k_s = 26.67 sec^{-1}).
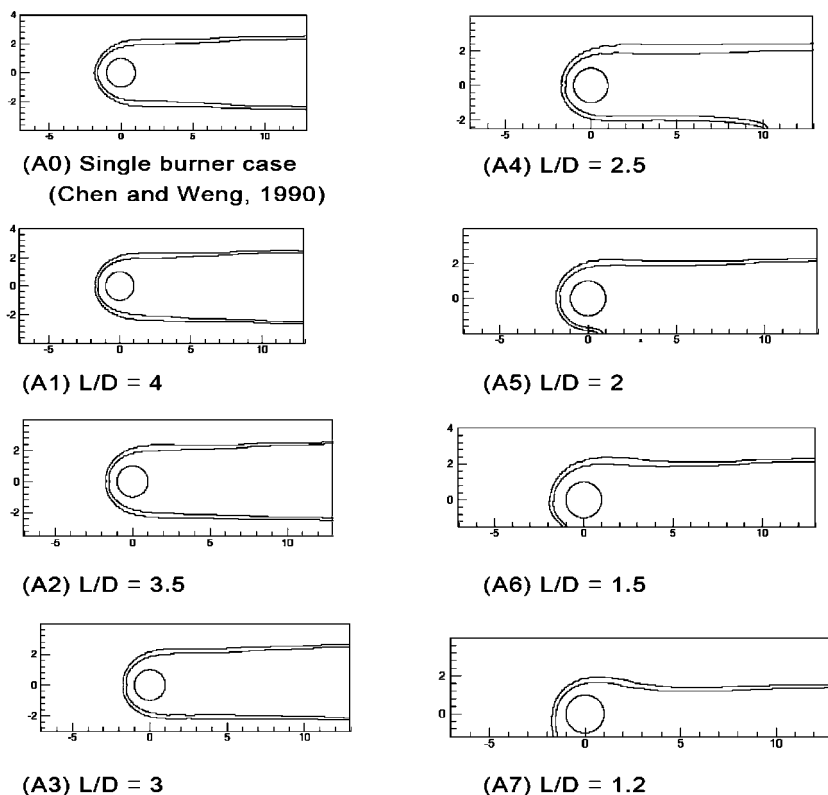
Figure 9. Series of $10^{-4}\,\text{g}/(\text{cm}^3 \times \text{sec})$ fuel reaction rate contours in $0.2\,\text{m}/\text{sec}$ inflow velocity condition (Re $= 17.75$ and $k_s = 26.67\,\text{sec}^{-1}$).

temperature (Figure 8-A1), reaction rate (Figure 9-A1), and fuel and oxygen mass fractions contours (Figure 10-A1) in the 4 D inter-cylinder separation distance case are all symmetric about the line, y $= 0$. Apparently, it indicates that absolutely no flame interference/interaction occurs in the case of a 4 D inter-cylinder separation.

Parametric Studies

Effect of Varying Inter-cylinder Spacing (L).
Combustion Efficiency: The combustion efficiency used in this study is defined as:

$$\text{Combustion efficiency} = \frac{\dot{m}_{O,\text{in}} - \dot{m}_{O,\text{out}}}{\dot{m}_{O,\text{in}}} \times 100,$$
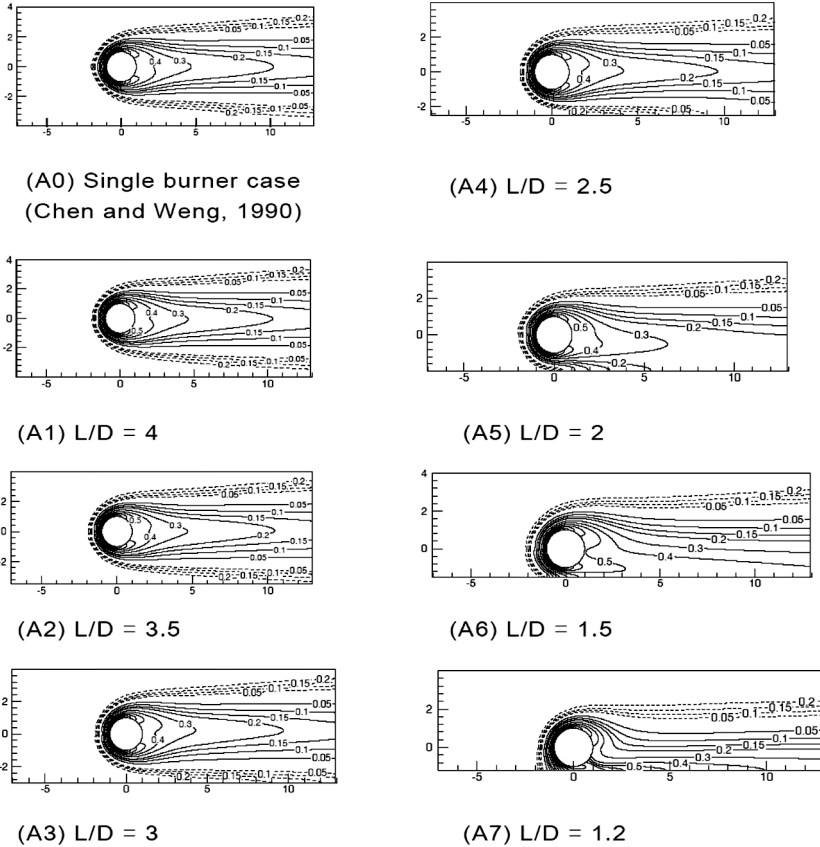
(A0) Single burner case
(Chen and Weng, 1990)

(A4) L/D = 2.5

(A1) L/D = 4

(A5) L/D = 2

(A2) L/D = 3.5

(A6) L/D = 1.5

(A3) L/D = 3

(A7) L/D = 1.2

Figure 10. Series of fuel and oxygen mass fraction contour distributions in 0.2 m/sec inflow velocity condition (Re = 17.75 and k_s = 26.67 sec^{-1}). (Solid lines are fuel mass fraction contour lines and dashed lines are oxygen mass fraction contour lines.)

where $\dot{m}_{O,in}$ is the total mass flow rate of oxygen that flows into the wind tunnel, and $\dot{m}_{O,out}$ is the corresponding one survived at the downstream boundary. It serves as an indicator of dual flame interaction/interference. Figure 11 shows the combustion efficiency as a function of inter-cylinder spacing. Notably, the combustion efficiency of the dual burners with a 3.5D inter-cylinder separation is the same as that in the single burner case, implying that the interaction/interference can be ignored when the separation is larger than or equal to 3.5D, whereas flame interaction/interference occurs when the inter-cylinder spacing is less than 3.5D. The value with an inter-cylinder separation distance of 3.5D is approximately
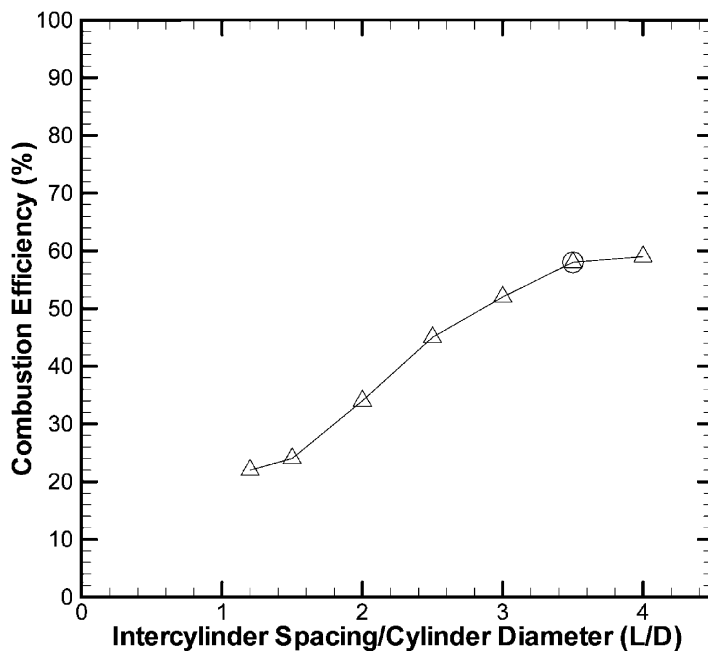
Figure 11. The combustion efficiency as functions of the intercylinder spacing. (The circle is the single burner result.)

2.4 times of that obtained with a distance of 1.5D. In the range $1.2 \leq L/D < 3.5$, the combustion efficiency increases with the inter-cylinder separation. It is because the air supply rate between burners is higher as the spacing is wider. The detailed flame structures will be given in next section.

Flames' Configurations and Interaction: When the inter-cylinder spacing is under 3.5 D, the flames interact with each other as shown in Figures 8-A3 ∼ 8-A7 and 9-A3 ∼ 9-A7. The dual envelope flame fronts merge completely when the inter-cylinder spacing is less than 2 D (Figure 8-A5). The merged flame front shows an anchor shape when the inter-cylinder spacing is between 1.5 D and 2.5 D (Figures 8-A4 ∼ 7-A6). The merged point moves toward upstream as the inter-cylinder separation is reduced. Upon L = 1.2 D, the flames that surround the dual cylinders become a single, wide envelope flame (Figures 8-A7 and 9-A7), and the two burners share a common wake. The flame characteristics of L = 1.5 D are similar to those of L = 1.2 D, except that the flame front is

slightly concave between the burners (Figures 8-A6 and 9-A6). The flame appears to have two "heads" and one "body" in the case of L = 2 D (Figures 8-A5 and 9-A5). When L exceeds 2 D, the envelope flame has two independent wakes. On the contrary, the envelope flame has only one wake when L is under 1.5 D. However, two dependent wakes are evident when L equals 1.5 D or 2 D. When L increases to 2.5 D, the dual envelope flame tails are connected far downstream (Figures 8-A4 and 9-A4). The flames appear to have two "bodies" and one "tail." (Figures 8-A4 and 9-A4.)

At L ≥ 3 D and, especially, 3.5 D, the dual envelope diffusion flames interact slightly (Figures 8-A2, 8-A3, 9-A2 and 9-A3). Thus, L = 3.5 D can be considered to be a critical inter-cylinder separation with respect to flame interaction, which also can be confirmed by the corresponding combustion efficiency mentioned in the last section. No flame interaction occurs at L = 4 D (Figure 8-A1). The dual flames at L = 4 D are fully independent of each other (Figures 8-A1 and 9-A1), and each individual flame is almost the same as that in the single Tsuji burner case (Figs. 8-A0 and 9-A0).

However, a larger high-flame-temperature region is yielded as the inter-cylinder spacing is increased (Figures 8-A1 ∼ 8-A7). The merged dual flames at a narrower inter-cylinder separation appear to be larger than each flame separated more widely. Therefore, the merging of the flames enlarges the flame but shrinks the high temperature region (Figures 8-A5 ∼ 8-A7). It is expected that the larger gap allows more oxidizer to flow into the region between the burners that let the flames on the inner side burn better. As the interspacing is reduced beyond the critical value, such as 3.5 D, the inner flame for each burner tends to lean toward symmetry line in order to catch more oxidizer to support itself. Then, the flame interference commences to show up as the burners become closer further. Because the reduction of oxidizer supply rate due to the smaller gap between burners, the high temperature region between burners becomes smaller. In the meantime, the flames seem enlarged due to the flame merging.

Combustion Flow Field: Two vortices are formed behind a burner when L ≥ 2.5 D (Figures 8-A1 ∼ 8-A4), bur only one vortex is present behind a burner when L is 1.5 D or 2 D (Figures 8-A5 and 8-A6). No vortex is formed behind eitherburner when L = 1.2 D (Figure 8-A7). In the last case, the streamlines in front of the burners are twisted,

because the two burners are too close to each other to allow the fluids to flow smoothly through the gap between the burners. In other words, the dual burners behaveas one large obstacle to the fluids. A wider inter-cylinder spacing yields smoother streamlines in front of the burners (Figures 8-A1∼8-A7). When it is sufficiently wide (Figures 8-A1 and 8-A2), the streamline pattern is very similar to that in the single burner case. Therefore, the interference becomes greater at a smaller inter-cylinder separation. The stagnation region in front of each cylinder shifts toward the symmetry line at $y = -L/2$ as the inter-cylinder separation is reduced (Figures 8-A1∼8-A7). The forward stagnation regions at $L = 3.5\,D$ and $4\,D$ (Figures 8-A1 and 8-A2) are consistent with that in the single burner case (Figure 8-A0). Therefore, theinteractions between burners can be ignored at a much larger inter-cylinder separation.

The location of the stagnation region/point on the front surface of the cylinder indicatesthe amount of fluid that flows through the gap between the burners. A narrower gap between the cylinders allows less fluid to flow through it. Therefore, the fluid passes through the gap with difficulty when $L = 1.2\,D$, $1.5\,D$, or $2\,D$ (Figures 8-A5∼8-A7), causing more fluidto flow downstream along the outer surfaces of the burners, and then sharply bend toward the centerline once they pass through the outer surface of the cylinder (Figures 8-A5∼8-A7). This phenomenon results in only a single vortex or no vortex behind each cylinder, and the flame interference is obvious in these three cases, too (Figures 8-A5∼8-A7).

Therefore, the number of vortices is an indicator of the strength of flame interaction/interference. When L is increased to $2.5\,D$, two vortices are found to rotate in opposite directions behind each burner (Figure 8-A4). The forward stagnation region approaches the front top zone of the burner (Figure 8-A4). The fluid smoothly bends toward centerline of the cylinder at $y = 0$, after passing through the burner's outer surface (Figure 8-A4). Although the tails of the two counterflow diffusion flames are connected to each other (Figures 8-A4 and 9-A4), the individual flow field is similar to that of the single burner (Figures 8-A0 and 9-A0).

Fuel and Oxygen Mass Fraction Distributions: The mass fraction contours of fuel and oxygen are presented as Figure 10. More fuel remains downstream at a smaller inter-cylinder separation (Figures 10-A5∼10-A7), because the burning of inner flames for these cases is poorer due to less oxidizer supply rate. The mass fraction contours of fuel are clearly not symmetric alongthe line $y = 0$ when $L = 1.2\,D$, $1.5\,D$

or 2 D (Figures 10-A5 ∼ 10-A7), so the dual flames obviously in those case-sinteract with each other. The oxygen deficiency between the flames is the primary cause of flame interaction. The profiles of fuel mass fractions appear somewhat symmetric about the y = 0 line at L = 2.5 D and 3 D, while the contours of oxygen mass fraction are not (Figures 10-A3 and 10-A4), especially at L = 2.5 D (Figure 10-A4). Thus, the interaction between flames is weak at L = 2.5 D and 3 D. As L increases above 3 D, the fuel and oxygen mass fraction contours become symmetric about the line y = 0 (Figures 10-A1 and 10-A2). Apparently, flame interaction phenomena do not occur at L = 3.5 D or 4 D (Figures 10-A1 and 10-A2).

Effect of Inflow Velocity (U_{in}). In this part, the interspacing between the burners is kept at L = 3 D and the inflow velocity varies from 0.2 m/s to 1.955 m/s.

Envelope Diffusion Flame: Two envelope flames surround the porous cylinders in the low-speed flow regime, in which the corresponding inflow velocity is under 0.79 m/sec. Cases B1, B2 and B3 in Figure 12 belong to this category.

As shown in Figures 12-B1, 12-B2 and 12-B3, the envelope diffusion flames seem to be situated around the front porous cylinder and spread downstream. The active reaction zones in Figures 13-B1, 13-B2, and 13-B3 also exhibit this feature. A flame of this type is identified as a diffusion flame, whose fuel side can be distinguished from its oxidizer one, as shown in Figures 14-B1, 14-B2 and 14-B3.

In Figure 12-B1, the maximum temperature along the front stagnation streamline is about 2118 K at x = −1.5. Similarly, it is 1785 K at x = −1.127 in Fig. 12-B2, and 1749 K at x = −1.109 in Fig. 12-B3. The isotherms above 600 K in front of the burner are almost parallel to the cylindrical surface because the fuel-ejection rate is uniform. Figures 12-B1, 12-B2 and 12-B3 verify this fact. Therefore, the flame stand-off distance can be regarded as constant along the fuel supply surface. This uniform fuel supply, in a direction opposite to that of the flow of the oxidizer, makes the concentration of isotherms on the oxidizer side higher than that on the fuel side in front of the cylinder. Just behind the surface through which the fuel is supplied, the isotherms are no longer parallel to the surface but are dispersed. The isotherms on the fuel side shift inward at the back of the cylinder and form a closed loop, since no blowing occurs there. Some lower isotherm envelopes, such as those of
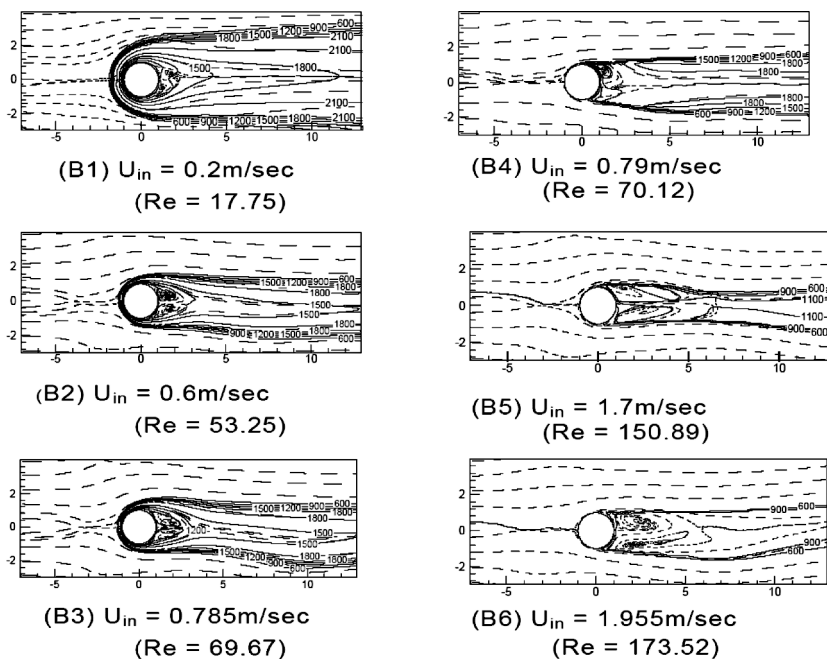
(B1) U$_{in}$ = 0.2m/sec
(Re = 17.75)

(B2) U$_{in}$ = 0.6m/sec
(Re = 53.25)

(B3) U$_{in}$ = 0.785m/sec
(Re = 69.67)

(B4) U$_{in}$ = 0.79m/sec
(Re = 70.12)

(B5) U$_{in}$ = 1.7m/sec
(Re = 150.89)

(B6) U$_{in}$ = 1.955m/sec
(Re = 173.52)

Figure 12. Series of streamline and temperature contour distributions in 3 D intercylinder spacing condition (L/D = 3).

$T = 900$ and $1200\,K$, are apparently affected by the recirculation flow in the wake, as illustrated in Figures 12-B1, 12-B2 and 12-B3. The isotherms on the oxidizer side initially move outward, and then spread to the wake (Figure 12-B1). Far downstream, where the influence of the recirculation is negligible, the temperature gradient in the cross-stream direction is found to be much greater than that in the direction of the stream.

In Figure 12-B1, where the inflow velocity is 0.2 m/sec, the tails of the $T = 600$ and $900\,K$ isotherms for the dual diffusion flames are connected to each other. The high temperature contours, such as those at $T = 1200$, 1500, 1800 and 2100 K, are slightly bent toward the wind-tunnel wall. In Fig. 12-B1, the two vortices behind the cylinder are extremely asymmetric. The lower vortex is closer to the cylinder than the upper one. However, the flame is almost symmetric in the line y = 0 (Figure 13-B1).

In Figure 14-B1, the contours of $Y_o = 0.15$ and 0.2 of the dual flames are connected. However, the intermediate Y_f contours, such as those of $Y_f = 0.2$, 0.3, and 0.4, are bent toward the tunnel wall. As the
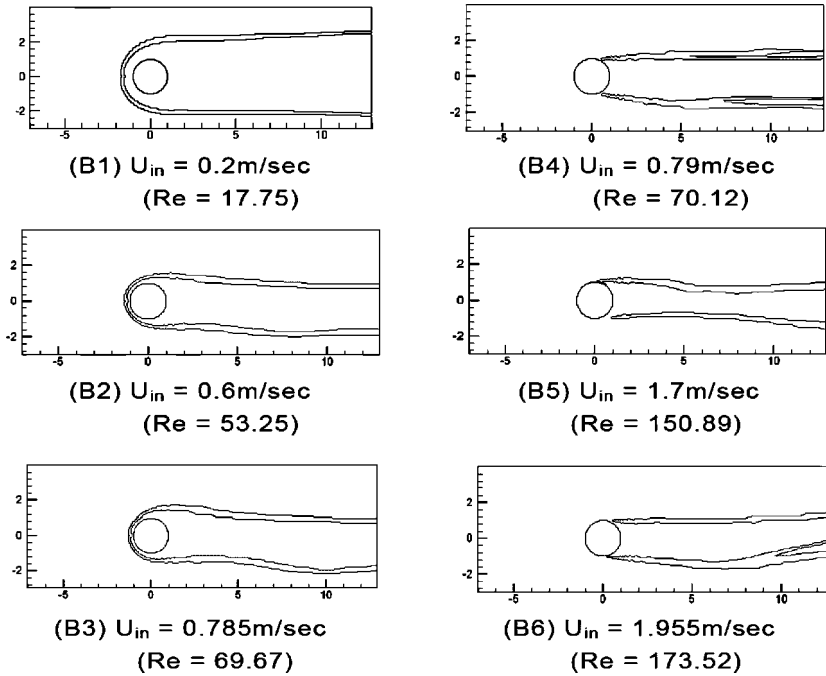
Figure 13. Series of 10^{-4} g/(cm^3 × sec) fuel reaction rate contours in 3D intercylinder spacing condition (L/D = 3).

inflow velocity increases to 0.6 m/sec or above, the wakes of the dual flames begin to bend toward each other (Figures 12-B2, 12-B3, 13-B2, and 13-B3). The maximum temperature is lower and the flame is smaller in Figure 12-B2 than in Figure 12-B1. The two sides of the downstream flame are almost parallel to each other in Figure 13-B2, but they are slightly divergent in Figure 13-B1. The streamlines in front of the burner twist enormously in Figures 12-B2 and 12-B3. The two vortices behind a cylinder are not the same size, as the lower vortex is slightly larger than the upper one. In Figure 14-B2, the Y_o and Y_f contours of the dual flames initially approach each other mid-downstream, but slightly diverge from each other far downstream.

Further increasing the inflow velocity to 0.785 m/sec causes the downstream flame to twist tremendously (Figures 12-B3 and 13-B3). The isotherms of the dual flames approach each other at x = 9.7, due to the interaction between the flames, but they are separate from each
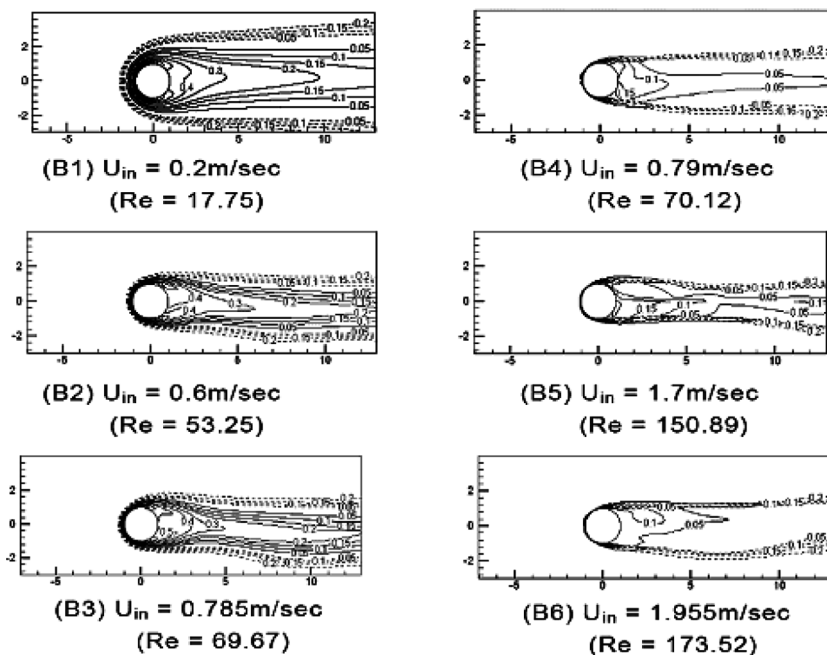
(B1) U$_{in}$ = 0.2m/sec
(Re = 17.75)

(B2) U$_{in}$ = 0.6m/sec
(Re = 53.25)

(B3) U$_{in}$ = 0.785m/sec
(Re = 69.67)

(B4) U$_{in}$ = 0.79m/sec
(Re = 70.12)

(B5) U$_{in}$ = 1.7m/sec
(Re = 150.89)

(B6) U$_{in}$ = 1.955m/sec
(Re = 173.52)

Figure 14. Series of fuel and oxygen mass fraction contour distributions in 3 D intercylinder spacing condition. (Solid lines are fuel mass fraction contour lines and dashed ones are oxygen mass fraction contour lines.)

other further downstream. The fuel reaction rate contour at 10^{-4} g/ (cm^3*sec), assigned as the flame boundary, in Figure 13-B3, shows a similar trend. The maximum temperature in Figure 12-B3 is lower than that in Figure 12-B2. Figure 12-B3 shows two nearly identical vortices behind a cylinder. The regions of recirculation flow in Figures 12-B2 and 12-B3 are larger than that in Figure 12-B1. However, the mass fraction contours of fuel and oxidizer in Figures 14-B2 and 14-B3 are similar. The distributions of isotherms and streamlines in Figures 12-B2 and 12-B3 are also similar. Figures 12-B1, 12-B2, 12-B3, 13-B1, 13-B2 and 13-B3, show that as the inflow velocity increases, the twisting of the flame becomes increasingly more severe. In the meantime, the tails of the dual flames tend to approach each other. Thus, the flame becomes more and more asymmetric, implying that increasing the inflow velocity enhances the interaction between the dual envelope diffusion flames.

Wake Flame: When inflow velocity is 0.785 m/sec, it is still an envelope flame. Followed by a small increment to 0.79 m/sec, it suddenly becomes a wake flame, as shown in Figure 12-B4. From $U_{in} = 0.785$ to 0.79 m/s, the flame fronts retreat from the front surfaces and eventually stabilize to the rear side of the cylindrical burners. Of course, the active reaction zones in Figure 13-B4 also exhibit the same feature. The flame attached to the rear side of burner is defined as a wake flame. Similar behaviors, as shown in Figures 12-B5, 12-B6, 13-B5, and 13-B6, are also observed as the flow velocity is increased further. The wake flame generated by the breakup of the envelope flame is due to the flame stretch effect, described next.

The breakup of the envelope flame in the front section of the cylinder causes a fuel-air mixture to exist in that region. The mixture is generated from the impingement of fuel and oxidizer streams that flow from opposite directions. Then, the mixture moves downstream by convection, and is ignited by the reversed hot combustion gas products in the vortex region, as shown in Figures 14-B4, 14-B5, and 14-B6. The flame front is near the top of the recirculation flow. The recirculation flow not only brings hot gases upstream from downstream to ignite the mixture, but also stabilizes the flame. This behavior resembles that of the bluff-body flame holder in after burner and ramjet systems. Note that the structure of the wake flame appears to be a premixed flame.

The maximum temperature in the whole computational domain is 1812 K in Figure 12-B4, 1186 K in Figure 12-B5 and 1048 K in Figure 12-B6. The maximum temperature of the wake flame decreases as the inflow velocity increases. In Figure 12-B4, all isotherms except the higher isotherms, such as T = 1500 and 1800 K, are nearly symmetric in the line y = 0. The high-temperature region is larger on the upper side of the wake flame than on the lower side. The 1500 K isotherm twists enormously at the region of recirculation flow, and almost passes through the centers of the two vortices behind the cylinder. It is strongly affected by the recirculation flow. The two vortices behind the burner have different sizes: the upper vortex is much larger than the lower one. The upper vortex attaches to the rear surface of the cylinder, but the lower vortex is separated from it (Figure 12-B4). The streamlines are smoother in the wake flame (Figure 12-B4) than in the envelope flame (Figure 12-B3). The gradient of the isotherms in the wake region of the wake flame is larger than that in the wake region of the envelope flame.

Figure 13-B4 reveals the fuel reaction rate contours, which represent the shape of the flame. The tails of this wake flame clearly diverge, from mid-downstream to far downstream. In Figure 14-B4, the amount of excess fuel in the wake region is less than in the case of the envelope diffusion flame (Figure 14-B3) due to thepremixing combustion. Therefore, the premixed flame burns more completely than the diffusion flame. Thus, the envelope flame and wake flame have extremely different combustion characteristics.

When the inflow velocity increases to $1.7 \, \mathrm{m/sec}$, the flame becomes thinner due to the flame stretch effect, but the recirculation flow zone becomes much larger than that in case B4 (Figures 12-B5 and 13-B5). The waist of the flame in case B5 is narrow, very unlike that in other cases. The two vortices behind the cylinder are approximately identical in size and shape, but the center of the upper vortex is closer to the rear surface of the cylinder (Figure 12-B5). The streamlines just in front of the cylinder twist severely. They contract at about $x = -2.73$ and then diverge immediately. Figures 12-B2 and 12-B3 depict similar behaviors. Additionally, the streamlines ahead of the cylinder in case B5 are not as smooth as those in B4.

The excess fuel in the wake region is more in Figure 14-B5 than in Fig. 14-B4, but still much less than in the wake regions ofall the envelope diffusion flames mentioned previously. The mass fraction contours of the fuel twist enormously in the wake region (Figure 14-B5). The region in which fuel and air are premixed extends much farther downstream than in case B4. Additionally, the $Y_f = 0.1$ contour occurring at far downstream is a very special phenomenon.

Increasing the inflow velocity to $1.955 \, \mathrm{m/sec}$, which is close to the extinction limit, causes the dual flames to diverge from each other far downstream, where streamlines are also divergent (Figures 12-B6 and 13-B6). The temperature of the flame in case B6 is lower than in all other cases. A larger inflow velocity corresponds to a lower flame temperature, which result is closely related to the flame stretch effect. However, three vortices are present behind the cylinder (Figure 12-B6), quite unlike in all other cases. In the cases of lower inflow velocity, twin vortices are formed behind a cylinder, which phenomenon can be retained over a very wide range of inflow velocities. As shown in Figure 12, the recirculation flow zones at higher inflow velocity are much larger than at lower velocity. In Figure 12-B6, the upper vortex is the largest one. The lower left vortex is larger than the other lower one. The lower two vortices are

strongly depressed by the upper vortex, so the lower vortices are slender. The lower right vortex twists severely. The streamlines are smoother in Figure 12-B6 than in Figure 12-B5.

In Figure 13-B6, the lower branch of the 10^{-4} g/(cm^3∗sec) fuel reaction rate contour diverges into two branches far downstream. This behavior is consistent with that in Figure 13-B4. With reference to the fuel and oxygen mass fraction contours, the fuel-air premixed area extends over mid-downstream (Figure 14-B6). The fuel is concentrated on the tunnel wall side of the cylinder, unlike in case B5. The mass fraction contours of oxygen of the dual flames bend away from each other far downstream. The distribution of the fuel mass fraction contour is more
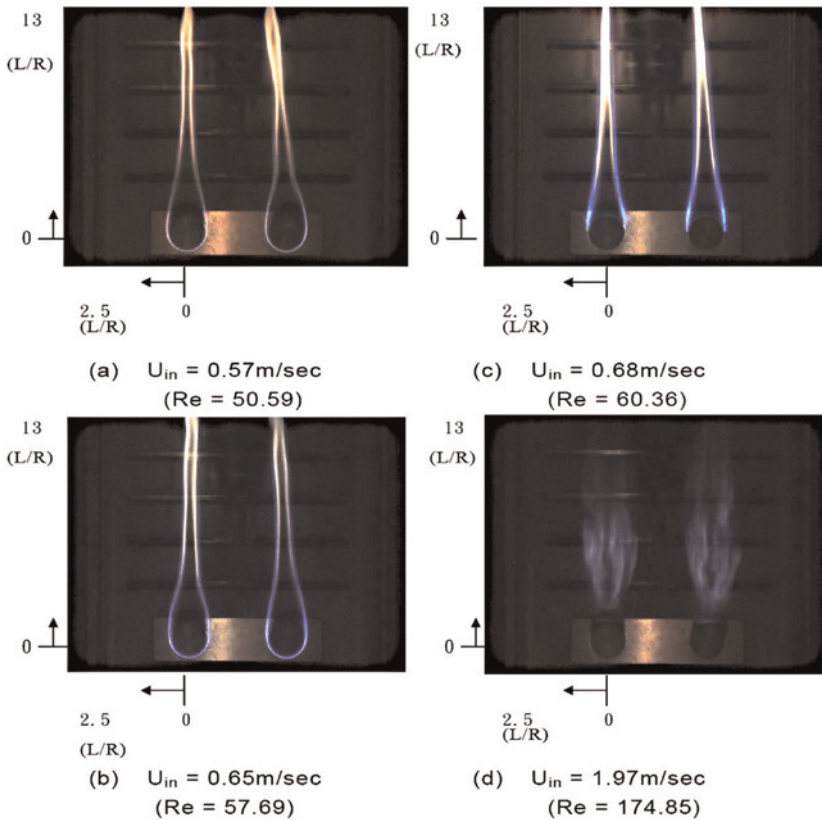

Figure 15. Series of flame configurations as a function of inflow velocity (L = 3 D, S = 360°, f_w = −0.1).

generally more asymmetric about the y = 0 line in cases that involve a wake flame than in cases that involve an envelope flame (Figure 14).

The whole process from the existence of the dual envelope flames to the existence of the dual wake flames as the inflow velocity increased is verified by Chen (2003). The flame configurations as a function of inflow velocity are recorded by a digital video camera (see Figure 6) in the whole process. Figure 15 presents the corresponding photographs, which can clearly demonstrate that the prediction and observation follow the same qualitative trends.

CONCLUSIONS

This work investigates the flame interference/interaction phenomena between two cylindrical burners arranged side-by-side. A multi-block grid system is used to implement the model, and one-step overall chemical kinetics mechanism is applied.

The comparisons between the flame transition curve in Wang (1998) and Chen's experiments (2003) are given separately, and the present simulation indicates that this simulation correctly predicts the trend for flame transition velocity with inter-cylinder spacing. Interesting parametric studies concern inter-cylinder spacing (L) and inflow velocity (U_{in}). For the interference between flames, a wider inter-cylinder spacing generally corresponds to a lower flame transition velocity, tending to transform the envelope flame into the wake flame. However, the combustion efficiency increases with L. The twin envelope diffusion flames merge into a larger envelope diffusion flame completely when L is equal to or less than 1.5 D. Only one vortex is present behind each burner when L = 1.5 D or 2 D. However, no vortex is present behind each burner when L = 1.2 D. When L is equal to or greater than 3.5 D, the two flames do not interfere with each other.

The mechanism of control of the interaction between twin counter-flow diffusion flames involves the oxygen deficiency between the dual flames. In the case of varying U_{in} at fixed L = 3D, the dual envelope diffusion flames are transformed into dual wake flames as U_{in} is increased to 0.79 m/sec. When U_{in} is further increased to 1.96 m/sec, the dual wake flames are extinguished. Increasing the inflow velocity promotes the interaction between dual envelope flames. A larger inflow velocity corresponds to a lower flame temperature, because of the flame stretch effect. Three vortices are present behind each cylinder near extinction,

quite unlike in which other cases. For fixed inter-cylinder spacing, the dual flames tend to attract each other normally. However, as the inflow velocity increases to the near-extinction limit, the dual flames repel each other. To summarize, the interaction between dual flames can be attractive or repulsive. Most flame interactions are attractive, and the latter kind is rare. The repulsion effect between dual flames does not occur when L is varied at constant inflow velocity. This special effect is counterintuitive, and worthy of further investigation in the near future.

NOMENCLATURE

$\overline{B}$ Frequency factor for gas phase reaction

C_p Average specific heat

D Cylinder diameter

$\overline{D}$ Dimensional species diffusivity

Da Damkohler number $\left(Da = \frac{R/U_{in}}{1/(\rho^* \overline{B} \exp(-\overline{E}/R^0 T^*))} \right)$

$\overline{E}$ Activation energy for gas phase reaction

f_w Non-dimensional fuel-ejection rate $\left(-f_w = \left(\frac{v_w}{U_{in}} \right) \left(\frac{Re}{2} \right)^{0.5} \right)$

k_s Flame stretch rate $\left(k_s = \frac{2U_{in}}{R} \right)$

L Inter-cylinder separation distance

Le Lewis number, $\overline{\alpha}/\overline{D}$

$\dot{m}$ Mass flow rate

P Pressure

ΔP Pressure correction

Pr Prandtl number, $\overline{\nu}/\overline{\alpha}$

$\overline{Q}$ Heat of combustion per unit mass of fuel

R Radius of cylinder

R^0 Universal gas constant

Re Reynolds number $\left(Re = \frac{\rho^* U_{in} R}{\mu^*} \right)$

S Fuel-ejection area (in degrees)

T Non-dimensional temperature

$\overline{T}_a$ Ambient temperature

T_w Non-dimensional wall temperature

T^* Reference temperature

U_{in} Incoming oxidizer velocity

U Non-dimensional velocity in x-direction

V Non-dimensional velocity in y-direction

v_w Fuel ejection velocity through surface of cylinder

x   Non-dimensional distance in x-direction

y   Non-dimensional distance in y-direction

Y_f Mass fraction of fuel

Y_o Mass fraction of oxidizer

Greek

α^* Thermal diffusivity at T^*

μ Dynamic viscosity

μ^* Dynamic viscosity at T^*

ν Kinematic viscosity

ρ Density

ρ^* Density at T^*

$\overline{\omega}$ Reaction rate

Overhead

–   Dimensional quantities

Superscript

*   Reference state

Subscripts

a   Ambient

f   Fuel

o   Oxidizer

in   Inflow position

out   Outflow position

n, t   Normal and tangential to cylinder surface

w   Surface of the porous cylinder

wall   Chamber wall

REFERENCES

Abdalla, V.R., Carvalho, Jr., J.A., and Ferreira, M.A. (1999) An investigation on parallel, divergent and convergent acetylene dual jet diffusion flames. *International Communication of Heat and Mass Transfer*, **26**, 8, 1151–1162.

Annamalai, K., Ryan, W., and Dhanapalan, S. (1994) Interactive processes in gasification and combustion–part III: Coal/Char particle arrays, streams and clouds. *Progress in Energy and Combustion Science*, **20**, 487–618.

Chen, C.-H. and Weng, F.-B. (1990) Flame stabilization and blowoff over a porous cylinder. *Combustion Science and Technology*, **73**, 427–446.

Chen, V.R. (2003) Experimental visualization and Measurements for Flame Interaction Between Dual Tsuji Burners in Side-by-side Arrangement. M.S. thesis, National Chiao Tung University, Taiwan.

Dong, L.L., Leung, C.W., and Cheung, C.S. (2003) Heat transfer of a row of three butane/air flame jets impinging on a flat plate. *International Journal of Heat and Mass Transfer*, **46**, 113–125.

Kharbat, E. (1992) Digital Image Processing Applications in the Ignition and ombustion of coal. M.S. Thesis, Texas A&M University, College Station, Texas, U.S.A.

Menon, R. and Gollahalli, S.R. (1985) Multiple jet gas flames in still air. *Heat Transfer in Fire and Combustion Systems*, **45**, 127–132.

Mohr, J.W., Seyed-Yagoobi, J., and Page, R.H. (1996) Heat transfer from a pair of radial jet reattachment flames. *ASME Heat Transfer Division*, **328**, 11.

Thomas, P.P. and Middecoff, J.F. (1980) Direct control of the grid point distribution in meshes generated by elliptic equations. *AIAA Journal*, **18**, 6, 652–656.

Tsa, S.S., Chang, C.C., and Chen, C.-H. (2005) Experimental visualizations of counterflow diffusion flame over a porous cylinder burner. *Journal of the Chinese Society of Mechanical Engineers*, **26**, 3 (in press).

Tsa, S.S. and Chen, C.-H. (2003) Flame stabilization over a Tsuji burner by four-step chemical reaction. *Combustion Science and Technology*, **175**, 2061–2093.

Toong, T.-Y. (1961) A theoretical study of interactions between two parallel burning fuel plates. *Combustion and Flame*, **5**, 221–227.

Tsuji, H. and Yamaoka, I. (1967) The counterflow diffusion flame in the forward stagnation region of a porous cylinder. Eleventh Symposium (International) on Combustion, The Combustion Institute, Pittsburgh, p. 979.

Umemura, A. (1994) Interactive droplet vaporization and combustion—approach from asymptotics. *Progress in Energy and Combustion Science*, **20**, 325–372.

Wang, J.-Y. (1998) The effect of Interaction Between Two Porous Flame Mechanism with Nitrogen ejector. M.S. Thesis, National Taiwan University, Taiwan.

Westbrook, C.K. and Dryer, F.L. (1981) Simplified reaction mechanisms for the hydrocarbon fuels in flames. *Combustion Science and Technology*, **27**, 31–43.

Xu, S.J. (1995) The Effect of Interaction Between Two Porous Envelope Flame and its Extinction Mechanism. M.S. Thesis, National Taiwan University, Taiwan.

Zdravkovich, M.M. (1977) Review of flow interference between two circular cylinders in various arrangements. *ASME Journal of Fluids Engineering*, **99**, 618–633.